PCCP

Accepted Manuscript




ROYAL SOCIETY OF CHEMISTRY

www.rsc.org/pccp

# Synthesis of Free-Standing, Curved Si Nanowires through Mechanical Failure of Catalyst during Metal Assisted Chemical Etching

Chang Quan Lai[1] and W. K. Choi[1,2,*]

[1]Advanced Materials for Micro- and Nano-Systems Programme, Singapore-MIT Alliance, Singapore 117583

[2]Department of Electrical and Computer Engineering, National University of Singapore, Singapore 117583

[*] Corresponding author; Email: elechoi@nus.edu.sg

## Abstract

The fabrication of orderly arrays of free-standing, curved Si nanowires over large areas (1cm x 1cm) was demonstrated by means of interference lithography and intentional mechanical failure of a perforated Au catalyst during metal assisted chemical etching. Photoresist microgrooves were deposited on the perforated Au film to cause uneven etching which resulted in the build-up of bending stresses in the Au film to the point of catastrophic failure. By considering the initial positions of the holes in the perforated Au film relative to the photoresist constraints, the precise location of the fracture can be predicted using simple beam mechanics. Therefore, the type of curved nanowires obtained can be designed with a high degree of reliability and control. Four distinct types of nanowire arrangements were demonstrated for this study.

## Introduction

The interest in nanotechnology over the last decade can be largely attributed to the unique properties materials display at the nanoscale level. These special properties can potentially be exploited in a wide variety of engineering devices and are often strongly dependent on the shape and form of the nanostructures. For instance, it is known that slight changes to the profile of nanoparticles (e.g. faceted, elongated, spherical) can vastly alter their catalytic[1], magnetic[1,2] and plasmonic properties[3]. On the other hand, anisotropic nanostructures in an array, such as nanochannels and nanofins, can be used to guide the development of cells[4,5] and influence the shape of liquid droplets[6–8].

Recently, it was found that bent nanowires can cause directional wetting[9], plasmonic losses[10] and changes in the semiconductor bandgap[11]. However, it is not immediately clear whether these properties arise because of the nanowire curvature or the presence of mechanical strain in the bent nanowires. In addition, there are also theoretical studies suggesting that the curvature of the nanowires can cause a reduction in their thermal conductivity[12]. Such modifications to the physical properties of nanowires has a direct effect on nanowire applications in electronics[13], energy[14] and thermal management[15,16].

Despite the importance of understanding the effect curvature has on the properties of nanowires, however, there are few experimental studies performed on such structures. A major reason for this is the difficulty of fabricating curved nanowires reliably with large yield. Although Hildreth *et al.* have recently shown that curved nanowires can be obtained by rotational metal assisted chemical etching (MACE) using asymmetric pads[17], it was clear from the design of the pads that dense arrays of curved nanowires could not be produced. Moreover, the patterns required were complex and requires the use of electron beam

lithography. Thus, the method employed by Hildreth *et al.* is not suitable for the production of large area and yield of curved nanowires for commercial and research purposes.

Here, we demonstrate an alternative processing route that is simple but effective in obtaining large, ordered arrays (1cm x 1cm) of free-standing, curved Si nanowires by means of interference lithography patterning and MACE. The perforated Au film, which acts as a catalyst in MACE, was designed, using simple beam mechanics, to fail at specific points during the MACE process so that the resultant halves of the film would undergo rotation and form curved nanowires.

## Experimental Procedures

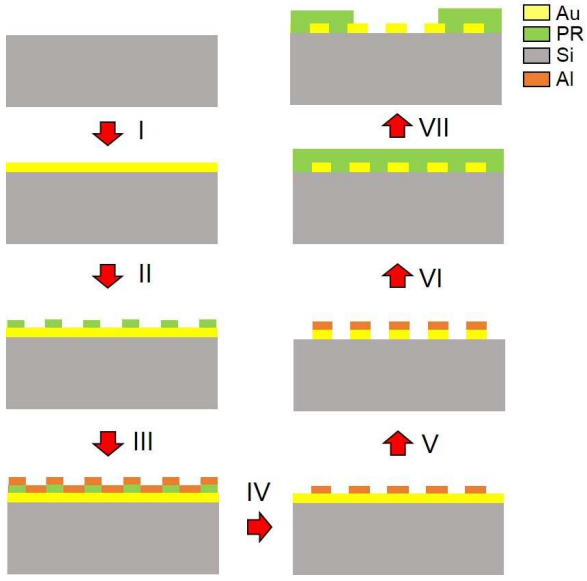


Figure 1: Schematic diagrams (side view) illustrating the fabrication of the perforated Au film covered with periodic PR microgrooves on a Si substrate.

P-type (100) Si wafers with resistivity of 4 – 8 Ω cm were first diced into 1cm x 1cm samples. After cleaning with RCA I, RCA II solutions and 10% buffered HF to remove the surface $SiO_2$, the desired thickness of Au was deposited onto the Si substrates at a pressure of $10^{-6}$ Torr using a thermal evaporator (Step I in Fig. 1). Although other metals such as Ag and Pt can be used as catalysts in MACE as well, Au was employed in this study because thus far, only the experimental values of the adhesion strength between Si and Au during MACE is known[18]. This information is important for theoretical calculations that will be presented later.

400nm of positive photoresist (PR), Ultra-i-123, was then spin-coated at 6000rpm onto the Au coated Si substrates and subjected to pre-exposure bake at 110°C for 90s. The samples were exposed twice, at right angles to each other, to an interference lithography system using a He-Cd laser (wavelength = 325nm) with a Llyod's mirror setup. Post exposure bake at 110°C was performed for 90s. After development with Microposit MF CD-26, a square array of PR nanodots was obtained on each sample surface (Step II). The period of the nanodots is 630nm while the diameter of each dot is 315nm.

Other than the fact that the interference lithography system can produce nanostructures at a very high yield, it should also be pointed out that it is used here because it produces uniform patterns, which allow the mechanical property of the metal catalyst to be consistent throughout, thereby making analysis easier and more accurate.

An Al film of thickness 90nm was then deposited onto the samples using the thermal evaporator system described above (Step III). After that, the samples were subjected to ultrasonication in acetone for 10min to remove the PR and Al coating on top of the PR, leaving behind a perforated Al film (Step IV). Following this, $CF_4$ plasma etching was carried

out at a rf power of 300W (at 13.56 MHz), pressure of 0.06 Torr and a flow rate of 10sccm to remove the exposed parts of the Au film (Step V).

The Al film was then removed with the CD-26 developer and 400nm of PR was spin-coated onto the surface again, following the steps listed above (Step VI). Using a mask aligner (SUSS MicroTec MJB4), the PR was exposed to UV light through a mask with periodic microgrooves that are 2μm wide and 2μm apart from each other. After post exposure baking at 110°C for 90s, the PR was developed in CD-26 to form periodic PR microgrooves on top of a perforated Au film that, in turn, laid atop a Si substrate (Step VII).

## Results and Discussion

When the samples were immersed in an etching solution containing 0.44M of $H_2O_2$ and 4.6M of HF, metal assisted chemical etching of Si began to take place (Fig. 2a). The perforated Au film acted as a catalyst, dissolving the Si immediately beneath it. The van der Waals' forces between the Au film and Si then caused the film to move down to occupy the space vacated by the dissolved Si[18]. Because the dissolution action was highly localized, the Si underneath the holes in the perforated films were not etched and thus, as the Au film sank into the Si, nanowires began to emerge through the holes in the perforated film.

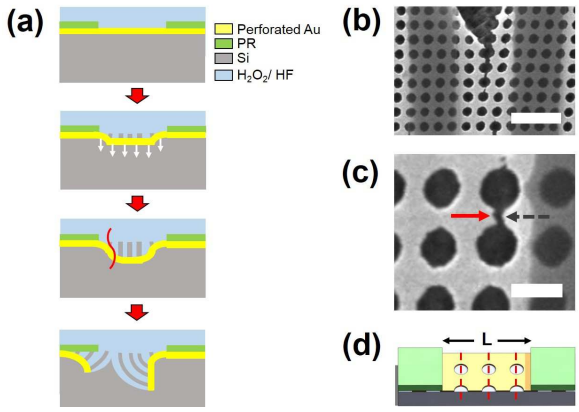


Figure 2: (a) Schematic diagrams illustrating the mechanical fracture and subsequent rotation of the perforated Au film to form curved nanowires during the MACE process. The white arrows represent the distributed adhesion force between Au and Si that is acting on the perforated Au film. The wavy red line indicates the point of fracture of the Au film which, in this case, is along the first row of holes. (b) SEM image of a fracture propagating through a row of holes for an Au film that is 20nm thick. The PR microgrooves show up as the darker regions in the image. (c) Magnified image of a crack passing through a row of holes. Cup (Red solid arrow) and cone (Black dashed arrow) fracture surfaces characteristic of ductile fracture is seen. (d) Schematic diagram illustrating a perforated Au beam between two adjacent microgrooves. Red dotted lines indicate the axes along which cracks will nucleate and propagate.

Since the etching solution has limited access to the Au film under the PR microgrooves, these parts of the Au film did not move down together with the exposed parts of the Au film, leading to bending stresses within the film. If these stresses become sufficiently large, catastrophic failure of the Au film will occur along one or more rows of holes in the perforated film (Fig. 2b) as these holes tend to concentrate the bending stresses in the film and thus, are more susceptible to yielding and fracture[19]. Once the Au film ruptures,

each of the two halves of the film will rotate about their respective PR constraints, leading to the formation of curved nanowires.

The mode of fracture observed in this case is ductile failure, evident from the cup and cone fracture surfaces (Fig. 2c), which is a clear indication that necking took place prior to mechanical failure. This observation is consistent with results reported for studies on the mechanical properties of thin Au films[20].

To obtain the desired arrays of curved nanowires, it is necessary to accurately designate the row of holes along which fracture should take place. To do this, we start by modelling a unit cell of the perforated Au film (schematic diagram shown in Fig. 2d) as a beam clamped at both ends, subjected to a force per unit area of $\rho$. The PR microgrooves, therefore, effectively segregates the entire Au film into independent beams of length $L$, which shall be referred to as the perforated Au beam from this point forth. $\rho$ arises as a result of the van der Waals' attraction between the Au film and Si substrate, and is the driving force for the deformation of the beam during MACE. The value of $\rho$ for the concentrations of $H_2O_2$ and HF used in this study was previously found to be approximately 2.5MPa[18].

The bending moment, $M$, experienced by such a beam can be given by[19]

$$M = \frac{\rho b}{12}\left(6Lx - L^2 - 6x^2\right), \text{ -------- (1)}$$

where $b$ is the width of the beam which is equivalent to the length of the microgrooves. $L$ refers to the length of the perforated Au beam (Fig. 2d) which is 2μm for this study, and $x$ refers to the distance between a point on the beam and the left PR microgroove clamp, which is selected as the reference point.

The maximum bending stress at any given point on this beam, $\sigma$, can be expressed as[19]

$$\sigma = \frac{MH}{2I} \text{ -------- (2)}$$

where $H$ refers to the thickness of the perforated Au beam and $I$ is the second moment of area of the beam along a row of holes (i.e. along the red dotted lines in Fig. 2d), which is given by

$$I = \frac{1}{24} bH^3 \text{ --------- (3)}$$

Notice that $b$, which is related to the width of the entire sample (1cm in this study), cancels out in Eq. (2). In other words, the maximum bending stress on any point on the Au film is independent of the total size of the sample.

For fracture to occur along a row of holes in the perforated Au beam, cracks must first nucleate at the edge of the holes. Given that the yield stress of Au is approximately 30GPa [21] for the thicknesses studied here (tens of nanometre), and considering that the circular holes concentrate stresses by a factor of 3 [19], the threshold bending stress for crack formation is 10GPa. In other words, if a row of holes is lined up at a point in the Au film where $\sigma \geq$ 10GPa, fracture can occur along the row of holes. Here, we have simplified the analysis by assuming that once the cracks nucleate at the holes, propagation of the cracks require no additional bending stresses i.e. it is assumed that no significant work hardening takes place during crack propagation.

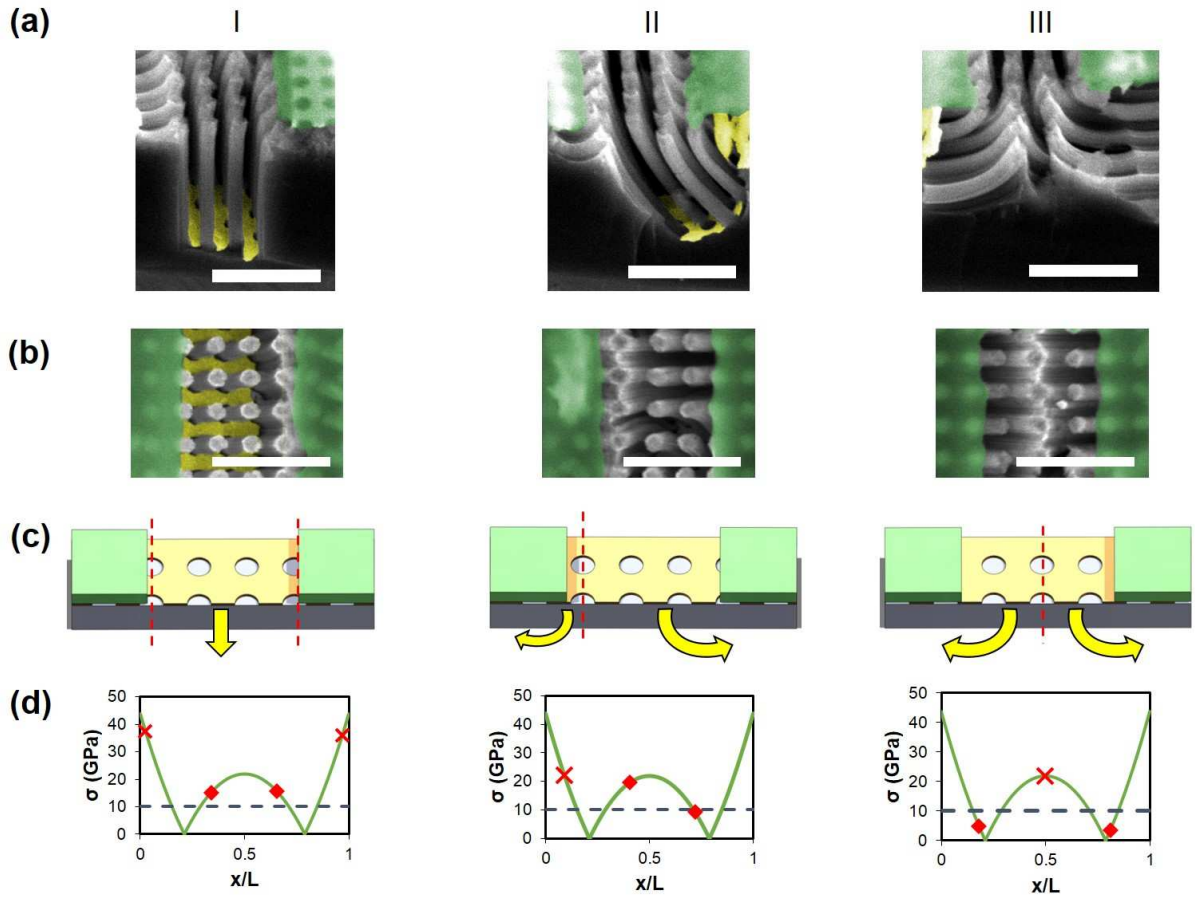


Figure 3: Results for a perforated Au film that is 15nm thick. (a) SEM images, taken at a tilted angle of 45°, of the different arrangements of nanowires that can be obtained. (b) Top views of the different nanowire arrangements. The PR microgrooves are coloured in green and the Au films in yellow for clarity. Scale bars represent 2μm. (c) Schematic diagrams illustrating the formation of each type of nanowires. The red dotted lines indicate the positions of the fractures and the yellow arrows show the subsequent rotation of the Au films. (d) $\sigma$ vs $x/L$ plots for the respective nanowire arrangements. The green curve represents the $\sigma$ values calculated for each point on the perforated Au beam while the red diamonds indicate the centres of the rows of holes that did not fracture. Red crosses denote the rows where a fracture had passed through. The dashed line indicates the threshold $\sigma$ for fracture to occur.

To verify our model, SEM images of the samples were taken after they have been subjected to MACE using the $H_2O_2$/ HF etching solution (Fig. 3a and b). The original positions of the holes relative to the PR microgrooves, indicated by the top of the curved nanowires, can be clearly seen. In addition, the row of holes where the fracture propagated through can be readily identified by the row of connected nanowires in Fig. 3b.

We have opted to use a system where the length of the perforated Au beam, *L*, is incommensurate with the period of the PR microgrooves for our experiments. The main advantage of this is that many different configurations of hole position relative to the PR microgrooves can be obtained on a single sample. For a perforated Au beam that is 15nm thick, these configurations lead to three general arrangements of curved nanowires (Types I - III) which are shown in Fig. 3.

Fig. 3c schematically illustrates the formation of each type of nanowires. For Type I nanowires, two fractures occur simultaneously near the ends of the perforated Au beam, close to the PR microgrooves. Because the resultant perforated Au film is free from any mechanical constraints, the distributed adhesion force between Au and Si will cause the film to move vertically downwards, leading to the formation of straight nanowires. For Type II nanowires, the fracture occurs near one of the edges of the Au beam so that it is split asymmetrically. The larger piece will then undergo rotation to form a larger number of curved nanowires that are also longer when compared to those formed by the smaller piece of perforated Au beam. For Type III nanowires, the fracture in the Au beam occurs through the middle row of holes, leading to two equal halves of the Au beam rotating in different directions and producing curved nanowires of similar length and curvature that face each other.

Plotting the positions of the holes shown in Fig. 3a and 3b on $\sigma$ vs *x/L* plots which can be calculated with Eqs (1) – (3), we were able to verify that indeed, fracture only occurs along rows of holes which have $\sigma \geq 10$GPa (marked by red crosses in Fig. 3d). However, the experimental results also indicate that Type I and Type II nanowires have rows of holes near the centre of the beam that did not fracture even though $\sigma \geq 10$GPa.

This can be easily explained once it is realized that as the perforated Au beam etches into the Si, $\sigma$ is first experienced at the ends of the Au beam near the PR constraints (Fig. 2a). As a result, before the rows of holes near the centre of the beam are subjected to their respective maximum bending stress, fracture would have already occurred at the ends of the perforated Au beam for Type I and Type II nanowires. Once failure of the Au beam takes place, all initial mechanical stresses within the beam are relieved and consequently, there is no fracture occurring along the other rows of holes in the perforated Au beam even if they were expected to have a maximum bending stress greater than 10GPa.

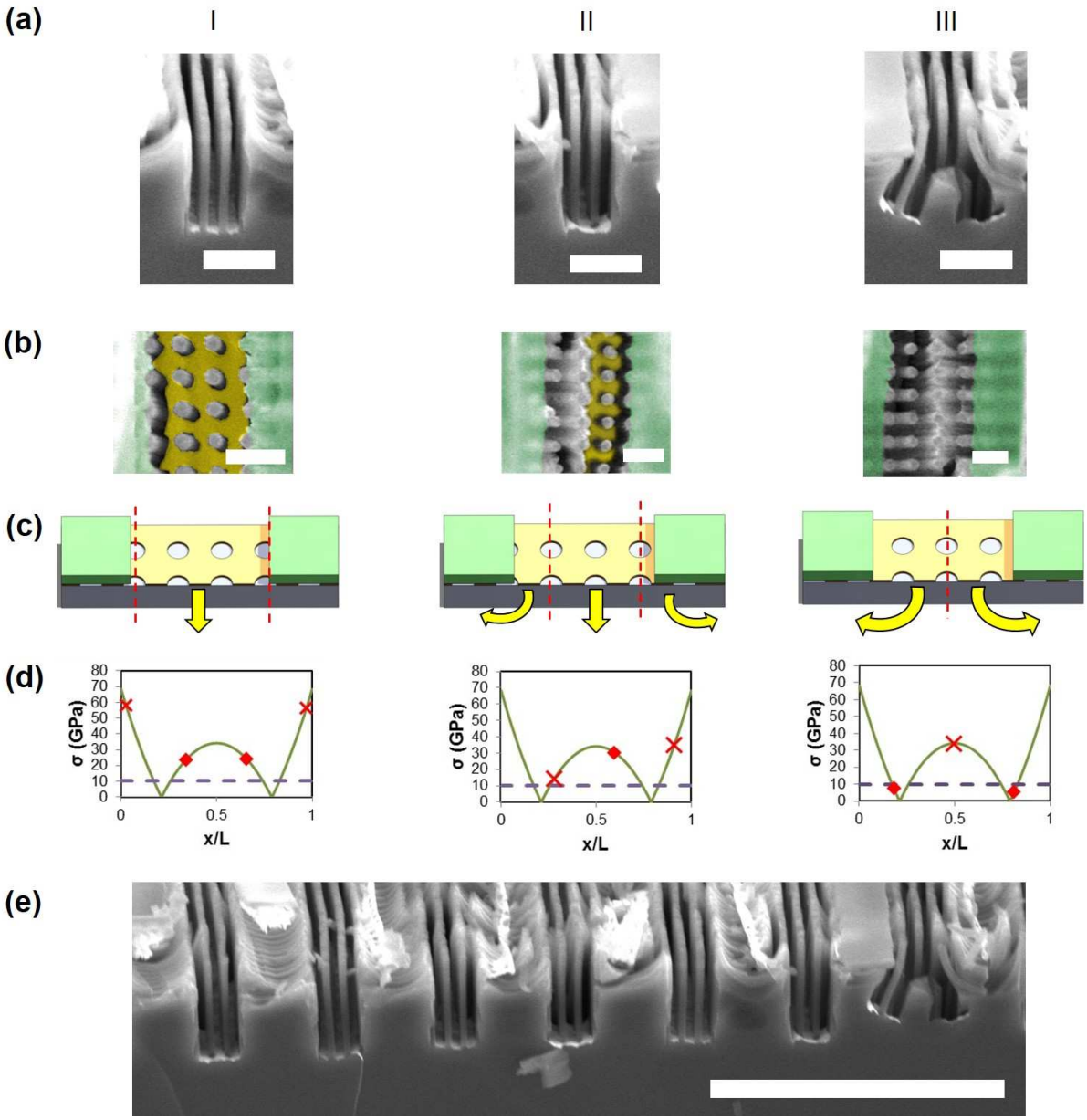


Figure 4: Results for a perforated Au film that is 12nm thick. All the items in the figure have the same meaning as those in Fig. 3. Enlarged sections of the image in (e) can be found in (a). Scale bar represents 2μm in (a) and (b) and 10μm in (e).

To further validate our model, we varied the thickness, and therefore, stiffness, of the perforated Au beam. Reducing the thickness of the Au beam from 15nm to 12nm yields three

general arrangements of curved nanowires also (Fig. 4). There are no changes for Type I and Type III nanowires observed for Au beams that are 12nm thick when compared to that observed for Au beams that are 15nm thick. There is, however, a slight difference for Type II nanowires. In this case, fracture takes place along two rows of holes instead of one due to the increase of $\sigma$ that is a direct result of a thinner perforated Au beam. Thus, the Au beam is split into three sections, with two yielding curved nanowires and one forming straight nanowires between the curved nanowires.

The biggest distinction between the nanowires obtained with 12nm of perforated Au beam as compared to 15nm of perforated Au beam is the significant lack of Type III nanowires observed with 12nm Au beam, as can be seen from Fig. 4e. This is because, the smaller thickness has caused $\sigma$ in the beam to rise so high that it becomes unlikely that rows of holes at the ends of the perforated Au beam would not experience a $\sigma$ value higher than 10GPa. To illustrate this fact, we note that 26% of the length of a perforated Au beam that is 15nm thick experiences $\sigma \leq$ 10GPa as compared to only 17% of an Au beam that is 12nm thick.

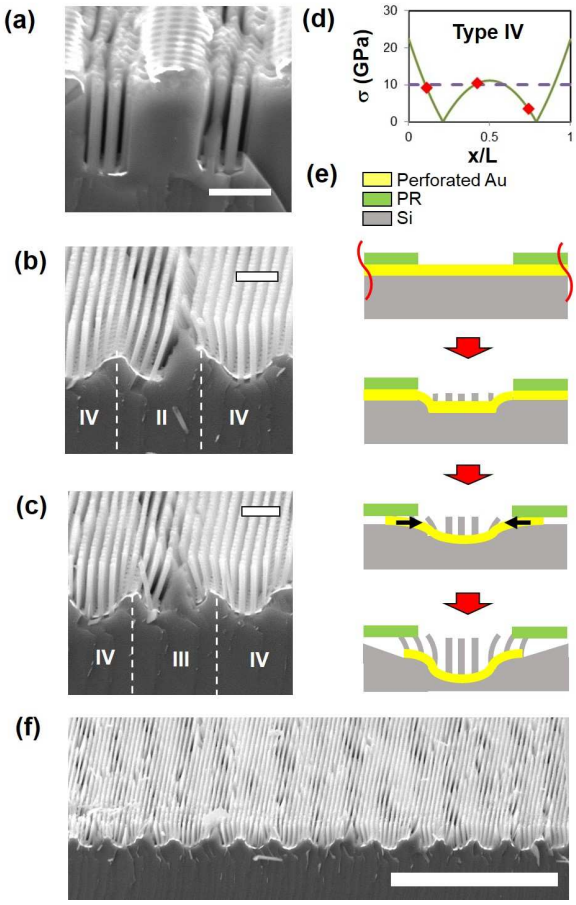


Figure 5: Results for a perforated Au film that is 20nm thick. (a) Type I nanowires. (b) Type II and Type IV nanowires. (c) Type III and Type IV nanowires. Scale bars represent 2μm. (d) Example of $\sigma$ vs $x/L$ plot for Type IV nanowires. (e) Schematic diagrams showing the formation of Type IV nanowires. Red wavy lines indicate the points of fracture while black arrows indicate the forces acting on the ends of the perforated Au beam. (f) SEM image of a section of the sample. Enlarged sections of the image in (f) can be found in (a) – (c). Scale bar represents 20μm.

On the other hand, if we were to increase the Au beam thickness to 20nm, a new arrangement of nanowires (Type IV) can be observed together with nanowires of Types I –

III (Fig. 5a-c). Unlike the other types of nanowires, however, fracture did not occur along any row of holes in the perforated Au beam for Type IV nanowires. The reason becomes clear once the positions of the holes for Type IV nanowires are plotted on the $\sigma$ vs $x/L$ graph (Fig. 5d) - the increased stiffness of the thicker Au beam lowers the $\sigma$ values in the beam to the extent where it becomes possible for $\sigma$ to fall below 10GPa for all the rows of holes in the perforated Au beam.

Fig. 5e shows the formation of nanowires of Type IV arrangement. Consider a Type IV perforated Au beam flanked by Type II perforated Au beams at its sides. Fractures will not occur within the Type IV Au beam but at the neighbouring Type II Au beams instead. The locations of the fractures are indicated by the red wavy lines. As a result, the Type IV Au beam etches into the Si substrate and pulls the ends of the beam underneath the PR towards the centre of the beam (pulling forces indicated by the black arrows in Fig. 5e). At the same time, the portion of beam under the PR constraints begins to delaminate from the PR as the etching solution undercuts the PR to cause MACE in these areas. Under the influence of these two effects, a Type IV perforated Au beam will eventually form a sinusoidal profile, with straight nanowires in its centre and curved nanowires at its ends (Fig. 5e). Note that unlike other types of curved nanowires which are formed by the rotation of a ruptured Au beam about a PR constraint, Type IV curved nanowires are caused by the localized translation and rotation of part of the Au beam. The slight rotation happens as the Au beam is adopting a sinusoidal profile, at points on the beam where the eventual gradient is not zero.

In addition, it is worth noting that in contrast to the results for Au beams of 12nm thickness, there is a lack of Type I nanowires observed for Au beams of 20nm thickness (Fig. 5f). Again, this is the direct result of a stiffer beam, which reduces the maximum bending stress on the beam and lowers the chances that the two rows of holes at the ends of the beam

will experience $\sigma \geq 10$GPa. As a comparison, holes in the region of $0 \leq x/L \leq 0.16$ will have $\sigma$ values greater than 10GPa for Au beams that are 15nm thick whereas they have to be in the region of $0 \leq x/L \leq 0.10$ on an Au beam that is 20nm thick to cross the threshold stress.

## Conclusion

In conclusion, we have demonstrated that curved Si nanowires can be fabricated through the purposeful fracture and subsequent rotation of a perforated Au film during MACE by means of photoresist constraints. The location of the fracture was shown to always occur along the centre of a row of holes, where the Au film is mechanically weakest due to the stress concentration effect. The particular row through which fracture will occur can be identified by calculating the maximum bending stress experienced by each row based on its position with respect to the photoresist constraints. In addition, for Au films where the period of the holes is incommensurate with the length of the perforated Au beams, a smaller film thickness will result in a much smaller proportion of curved nanowires whereas an overly thick film will deform into a sinusoidal shape, leading to the formation of alternating sections of curved and straight nanowires.

## Acknowledgements

The authors would like to acknowledge the partial funding of this work by the Singapore-MIT Alliance. Chang Quan Lai would like to express his deepest gratitude to the Singapore-MIT Alliance for the provision of research scholarship.

## References


1. Li, Y. *et al.* Well shaped $Mn_3O_4$ nano-octahedra with anomalous magnetic behavior and enhanced photodecomposition properties. *Small* **7,** 475–483 (2011).
2. Smolensky, E. D. *et al.* Scaling laws at the nanosize: the effect of particle size and shape on the magnetism and relaxivity of iron oxide nanoparticle contrast agents. *J. Mater. Chem. B* **1,** 2818–2828 (2013).
3. Nehl, C. L. & Hafner, J. H. Shape-dependent plasmon resonances of gold nanoparticles. *J. Mater. Chem.* **18,** 2415–2419 (2008).
4. Zhu, M. *et al.* Creation of nanostructures by interference lithography for modulation of cell behavior. *Nanoscale* **3,** 2723 – 2729 (2011).
5. Hu, W., Yim, E. K. F., Reano, R. M., Leong, K. W. & Pang, S. W. Effects of nanoimprinted patterns in tissue-culture polystyrene on cell behavior. *J. Vac. Sci. Technol. Vac. Surf. Films Off. J. Am. Vac. Soc.* **23,** 2984–2989 (2005).
6. Lai, C. Q., Thompson, C. V. & Choi, W. K. Uni-, Bi-, and Tri-Directional Wetting Caused by Nanostructures with Anisotropic Surface Energies. *Langmuir* **28,** 11048–11055 (2012).
7. Lai, C. Q. *et al.* Influence of nanoscale geometry on the dynamics of wicking into a rough surface. *Appl. Phys. Lett.* **102,** 053104–053104–4 (2013).
8. Kusumaatmaja, H., Vrancken, R. J., Bastiaansen, C. W. M. & Yeomans, J. M. Anisotropic Drop Morphologies on Corrugated Surfaces. *Langmuir* **24,** 7299–7308 (2008).
9. Chu, K.-H., Xiao, R. & Wang, E. N. Uni-directional liquid spreading on asymmetric nanostructured surfaces. *Nat Mater* **9,** 413–417 (2010).
10. Wang, W., Yang, Q., Fan, F., Xu, H. & Wang, Z. L. Light Propagation in Curved Silver Nanowire Plasmonic Waveguides. *Nano Lett.* **11,** 1603–1608 (2011).

11. Xue, H. *et al.* Probing the strain effect on near band edge emission of a curved ZnO nanowire via spatially resolved cathodoluminescence. *Nanotechnology* **21,** 215701 (2010).
12. Liu, L.-C., Huang, M.-J., Yang, R., Jeng, M.-S. & Yang, C.-C. Curvature effect on the phonon thermal conductivity of dielectric nanowires. *J. Appl. Phys.* **105,** 104313 (2009).
13. Chang, S., Oh, J., Boles, S. T. & Thompson, C. V. Fabrication of silicon nanopillar-based nanocapacitor arrays. *Appl. Phys. Lett.* **96,** 153108–153108–3 (2010).
14. Chan, C. K. *et al.* High-performance lithium battery anodes using silicon nanowires. *Nat Nano* **3,** 31–35 (2008).
15. Mai, T. T. *et al.* Dynamics of Wicking in Silicon Nanopillars Fabricated with Interference Lithography and Metal-Assisted Chemical Etching. *Langmuir* **28,** 11465–11471 (2012).
16. Zhang, C. & Hidrovo, C. H. Investigation of Nanopillar Wicking Capabilities for Heat Pipes Applications. *Proceedings of ASME 2009 Second International Conference on Micro/Nanoscale Heat and Mass Transfer* **3**, 423–437 (2009).
17. Hildreth, O. J., Brown, D. & Wong, C. P. 3D Out-of-Plane Rotational Etching with Pinned Catalysts in Metal-Assisted Chemical Etching of Silicon. *Adv. Funct. Mater.* **21,** 3119–3128 (2011).
18. Lai, C. Q., Cheng, H., Choi, W. K. & Thompson, C. V. Mechanics of Catalyst Motion during Metal Assisted Chemical Etching of Silicon. *J. Phys. Chem. C* **117,** 20802–20809 (2013).
19. Beer, F. P., Jr, E. R. J. & DeWolf, J. T. *Mechanics of Materials*. (McGraw Hill Higher Education, 2005).
20. Huh, Y.-H. *et al.* Observation of Micro-Tensile Behavior of Thin Film TiN and Au using ESPI Technique. *MRS Online Proc. Libr.* **875,** null–null (2005).

21. Avilés, F., Llanes, L. & Oliva, A. I. Elasto-plastic properties of gold thin films deposited onto polymeric substrates. *J. Mater. Sci.* **44,** 2590–2598 (2009).

## Table of Contents Graphic

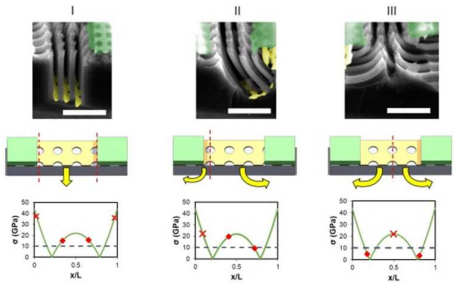


Perforated metal films on Si are designed to tear and rotate during etching, leading to curved nanowire formation.